Geophysical Journal International

Geophys. J. Int. (2020) **222,** 2108–2120
Advance Access publication 2020 June 12
GJI General Geophysical Methods

doi: 10.1093/gji/ggaa287

Joint detection and classification of rockfalls in a microseismic monitoring network

Liang Feng, Veronica Pazzi, Emanuele Intrieri, Teresa Gracchi and Giovanni Gigli

Department of Earth Science, University of Florence, Florence, Italy. E-mail: liang.feng@unifi.it

Accepted 2020 June 6. Received 2020 April 1; in original form 2019 August 30

SUMMARY

A rockfall (RF) is a ubiquitous geohazard that is difficult to monitor or predict and poses a significant risk for people and transportation in several hilly and mountainous environments. The seismic signal generated by RF carries abundant physical and mechanical information. Thus, signals can be used by researchers to reconstruct the event location, onset time, volume and trajectory, and develop an efficient early warning system. Therefore, the precise automatic detection and classification of RF events are important objectives for scientists, especially in seismic monitoring arrays. An algorithm called DESTRO (DEtection and STorage of ROckfalls) aimed at combining seismic event automatic detection and classification was implemented ad hoc within the MATLAB environment. In event detection, the STA/LTA (short-time-average through long-time-average) method combined with other parameters, such as the minimum duration of an RF and the minimum interval time between two continuous seismic events is used. Furthermore, nine significant features based on the frequency, amplitude, seismic waveform, duration and multiple station attributes are newly proposed to classify seismic events in a RF environment. In particular, a three-step classification method is proposed for the discrimination of five different source types: RFs, earthquakes (EQs), tremors, multispike events (MSs) and subordinate MS events. Each component (vertical, east–west and north–south) at each station within the monitoring network is analysed, and a three-step classification is performed. At a given time, the event series detected from each component are integrated and reclassified component by component and station by station into a final event-type series as an output result. By this algorithm, a case study of the seven-month-long seismic monitoring of a former quarry in Central Italy was investigated by means of four triaxial velocimeters with continuous acquisition at a sampling rate of 200 Hz. During this monitoring period, a human-induced RF simulation was performed, releasing 95 blocks (in which 90 blocks validated) of different sizes from the benches of the quarry. Consequently, 64.9 per cent of EQs within 100 km were confirmed in a one-month monitoring period, 88 blocks in the RF simulation were classified correctly as RF events and 2 blocks were classified as MSs given their small energy. Finally, an ad hoc section of the algorithm was designed specifically for RF classification combined with EQ recognition. The algorithm could be applied in slope seismic monitoring to monitor the dynamic states of rock masses, as well as in slope instability forecasting and risk evaluation in EQ-prone areas.

Key words: Fourier analysis; Instability analysis; Time-series analysis; Seismic noise.

1 INTRODUCTION

Rockfalls (RFs), or rock falls according to Hungr *et al.* (2014), are unstable processes consisting of the intermittent and rapid mobilization of various sizes, types and volumes of rock. These events are difficult to observe directly and pose significant risk for human habitation, security and transportation. Related to other natural disasters, the International Disaster Database suggests that between 1990 and 2015 landslides account for 4.9 per cent of all-natural disaster events and 1.3 per cent of all nature hazard fatalities. In total 55 997 people were killed in 4862 distinct landslide events from 2004 January to 2016 December (Froude & Petley 2018). There are many established approaches for detecting RF activity, and recently, characterization and monitoring have been carried out by passive seismic techniques (La Rocca *et al.* 2004; Lin *et al.* 2010; Feng 2011; Hibert *et al.* 2011; Yamada *et al.* 2012; Hibert *et al.* 2014;

Dammeier *et al.* 2016; Van Herwijnen *et al.* 2016; Coviello *et al.* 2019; Guinau *et al.* 2019; Li *et al.* 2019; Matsuoka 2019; Pazzi *et al.* 2019; Zhang & He 2019). The seismic signals generated by geomorphic processes (i.e. tectonic, climatic and anthropogenic activities) propagate from sources through the earth (Burtin *et al.* 2014; Fan *et al.* 2019) carrying abundant information about the event and allowing researchers to reconstruct the event location, onset time, volume, trajectory and so on (e.g. Manconi *et al.* 2016; Gracchi *et al.* 2017; Hibert *et al.* 2017; Arosio *et al.* 2018). Therefore, precise automatic event detection and classification are necessary in correlation analyses involving seismic events and environmental features (Helmstetter & Garambois 2010; Kortstrom *et al.* 2016).

There are two basic algorithms generally used in seismic event detection. (1) The most popular and widely used method, which was proposed by Allen (1978) and Trnkoczy (1998), is the short-time-average through long-time-average trigger (STA/LTA) algorithm. It continuously calibrates the average absolute amplitude of a seismic signal in two consecutive moving windows. This algorithm is applied in Kinemetric K2 firmware and Geopsy software (Trnkoczy 1998; Picotti *et al.* 2017). (2) The second algorithm is the cross-correlation, which is widely used in similarity analyses of data sets for two signals, images, sounds, etc. to recognize specific patterns. This method calculates the covariance between two traces to detect seismic events (it is a measurement of similarity as a function of the lag of one relative to the other). The final value of cross-correlation falls between -1 and $+1$. In real-world data, values $= \pm 1$ can never be achieved, and the absolute value will fall somewhere between these values, with a high value indicating a high degree of signal similarity and a low value indicating little similarity (Bendat & Piersol 2000; Yang *et al.* 2009; Akhouayri *et al.* 2014). Yang *et al.* (2009) proposed a waveform template matching method based on cross-correlation that is useful for the detection of the events that could provide a universal waveform template, such as for earthquakes (EQs) with clear and regular seismic waveforms. In the literature, there are also many other algorithms employed in seismic event detection, but most of them are modified from the aforementioned two basic algorithms. For example, there are algorithms that use denoising filters (Panagiotakis *et al.* 2008; Küperkoch *et al.* 2010; Rodriguez 2011; Gibbons *et al.* 2012; Akram & Eaton 2016), such as wavelet transforms (Hafez *et al.* 2009, 2010; Rodriguez 2011), that can remove useless noise from the original signal to obtain a stationary and clean signal for subsequent research. Notably, (i) an RF is characterized by multi-impact/rebound characteristics, irregular spike waveforms and a geomorphology-dependent duration; therefore, it is difficult to find a universal template waveform for cross-correlation, as proposed by Yang *et al.* (2009), but it is better to detect all events first and then classify them into different event types with seismic features; and (ii) denoising filters applied before data processing avoid the removal of important information.

Concerning seismic event classification, there are now many new approaches (hidden Markov models: HMM, neural networks, support vector machines, random trees, fuzzy logic, clustering, etc.) that have been tested and work well for seismic data with multiple purposes. For example, HMMs were initially introduced and studied in the late 1960s and early 1970s for speech recognition (Rabiner 1989). HMM recognition is based on the spectral properties of signals and the transformation of raw data into a parametric representation. Benítez *et al.* (2007) applied an HMM in seismic event classification for a volcano. For the HMM architecture, they designed in total 39 features relative to the energies in given frequency bands of the seismic signal, and they also performed training with a standard database for each event category. Heck *et al.* (2018) applied an HMM for snow avalanche precursor detection and classification, defined six features (central frequency, dominate frequency, instantaneous bandwidth, instantaneous frequency, cepstral coefficients and half-octave bands), and then trained one model for detection. HMMs are efficient tools for seismic event classification in real time with high accuracy, but they largely depend on the quality of the training model and the features defined, especially when only one component is applied. The HMM accuracy could be improved with the use of more seismic features, such as the ratio of the frequency or amplitude at two different seismic stations and the energy variations between different frequency bands, as proposed in this study. A neural network defines many key seismic features to create and train a model using a standard database to obtain a weight for each feature or an empirical function to describe these features (Romeo 1994; Scarpetta *et al.* 2005; Curilem *et al.* 2009; Akhouayri *et al.* 2015; Provost *et al.* 2017). Provost *et al.* (2017) proposed a random tree defined by 71 features that included the seismic signal waveform, spectrum, spectrogram, network geometry and polarity. Vallejios & McKinnon (2013) defined 29 features for event classification, such as the seismic energy, frequency, magnitude and some mechanical parameters estimated in the event motion process. For success detection and classification, the most important step is to build a good training database and define suitable seismic features, including not only the characteristics of the signal but also taking into account all the seismic stations parts of a monitoring network.

In this study, an ad hoc algorithm/procedure, DESTRO (DEtection and STorage of ROckfalls), for RF detection and classification, that makes full use of a monitoring array with a three-step designed classifier, was proposed. The whole algorithm can be segmented in three steps: (1) events detection, (2) seismic features calibration and (3) input the features into a three-step classifier. The presented application of DESTRO is based on a small-scale seismic network that monitored an unstable rock slope in a former limestone cave at Torgiovannetto (near Assisi, central Italy; Fig. 1) for seven months (Lotti *et al.* 2015; Gracchi *et al.* 2017; Lotti *et al.* 2018). To calibrate the system, 95 rock blocks were manually released from the benches of the former cave to simulate the occurrence of RFs, of which 90 were used for validation (Gracchi *et al.* 2017; Feng *et al.* 2019, 2020). The occurrence of EQs was cross-checked with the Italian National Institute of Geophysics and Volcanology (INGV) EQ database (http://cnt.rm.ingv.it/). For brevity, we do not present the seismic monitoring layout or the RF *in situ* test, but we invite the reader to refer to the literature, where more information can be found (Lotti *et al.* 2015; Gracchi *et al.* 2017; Lotti *et al.* 2018; Feng *et al.* 2019).

2 EVENT DETECTION

In this study, two methods, the STA/LTA and cross-correlation algorithms (specifically the maximum normalized cross-correlation method: MNCC), are compared to evaluate the most suitable alternative for DESTRO. It is important to note that in this work, and thus in DESTRO, to enhance amplitude changes, STA/LTA takes into account the average values of squared amplitudes, as suggested by Allen (1982), instead of the average values of the absolute amplitudes, as proposed by Trnkoczy (1998). MNCC consists of scanning the signal step by step in the time domain with two continuous sliding windows of the same length T and

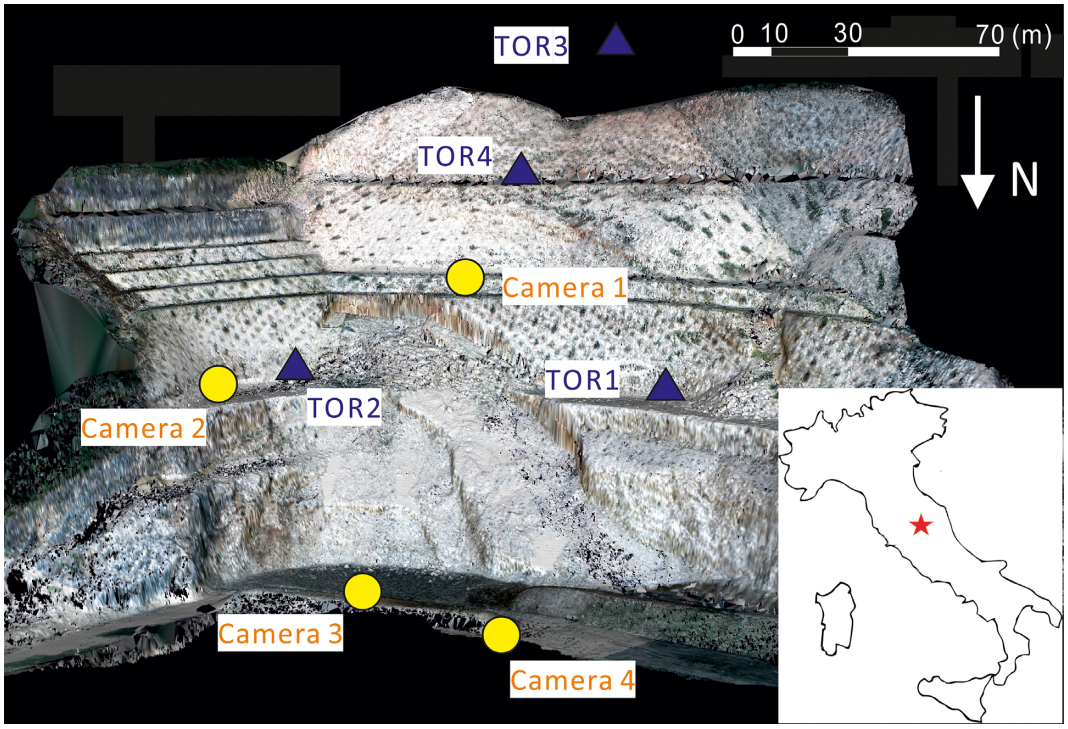

Figure 1. The LiDAR scanning digital elevation model of Torgiovannetto cave with the locations of the seismic stations (the blue triangles, named TOR 1, TOR 2, TOR 3 and TOR 4) and the cameras (yellow dots, named Camera 1, Camera 2, Camera 3 and Camera 4). In the box on bottom right, the red star is Assisi (central Italy).

sliding pitch θ; one sliding window is the master window in MNCC (Akhouayri *et al.* 2014). The degree of similarity between the two windows is continually examined by computing the MNCC value. If the two windows contain only background noise, the MNCC value does not vary significantly as t varies in the sense of MNCC $\geq \delta$ (threshold). Otherwise, the arrival of the P wave implies a notable downward variation in MNCC, which tends to be zero, and hence, MNCC $< \delta$ (threshold). The value of MNCC lies between 0 and 1, and a high value indicates a high degree of signal similarity.

To compare the detection methods, a short signal trace (270 s long), that contains two strong events and three weak events (marked with green ellipses in Figs 2 and 3), is analysed with both the STA/LTA and MNCC methods. This trace is extracted from the seven-month monitoring data set and chosen for this test due to its clarity. As clearly visible from the Torgiovannetto seismic traces, RFs bounce on the benches and every rebound is recorded by the seismic network as an impact (Gracchi *et al.* 2017; Feng *et al.* 2019).

With respect to the observation of the manually released RFs, the shortest length of one impact (the time at which the block impacts the slope surface) is 0.4 s, and 99.2 per cent (a value which covers most RF lengths and considers the lowest error) of the length of one whole RF event is less than 14 s. Therefore, the lengths of the short-time window and long-time window in DESTRO are chosen as 0.4 and 14 s, respectively. Fig. 2 shows the seismic event detection result and computational parameters for the STA/LTA method. Fig. 2(a), in particular, is the original signal trace, and the red lines are the onset times of each event automatically detected by STA/LTA; additionally, the dashed green ellipses are the manually selected events. Fig. 2(b) shows the two computational variables: the average energy over a short-time window (STA) and long-time window (LTA). Fig. 2(c) shows the two STA/LTA thresholds employed. The first threshold (*threshold 1*), used for event detection, was fixed at 4, and the second (*threshold 2*), which was used for checking the onset times of the events, was set equal to 2. The difference between the two thresholds is used to precisely select the event onset time. In the automatic STA/LTA event detection example shown in Fig. 2, four events are detected, and one weak event is missed (highlighted by the second green ellipse in Fig. 2a), since the two events are too close one to each other. The interval between them is indeed less than 2800 samples (i.e. 14 s), that was set as the minimum interval time between two separate events in DESTRO. However, this does not mean that DESTRO failed to detect events. In fact, if one component fails, there are many components defined in DESTRO, which are introduced and discussed in the next section. In the STA/LTA method, the values of the thresholds and lengths of the two windows are not permanent, and the most appropriate value should be modified depending on the monitoring site conditions and the types of target events (Trnkoczy 1998).

Fig. 3 illustrates the results of the MNCC method for the same original signal as the one used for STA/LTA. In Fig. 3(b), the black line is the value of the MNCC calculated with a moving window of 20 s and a step of $\theta = 0.005$ s; the blue dashed line is the MNCC mean value; and the red dashed lines are the detection thresholds suggested by Akhouayri *et al.* (2014), which are equal to the mean MNCC plus and minus the standard deviation (STD) of the MNCC mean value (mean $\pm$ STD). The red solid lines in Fig. 3(b) are the event onset times detected by the MNCC using mean $-$ STD according to the method suggested by Akhouayri *et al.* (2014). As a result, there are eight events detected by the MNCC, but only two of them (the second and the sixth ones) have been detected correctly. Notably, some events are missed, and some other are

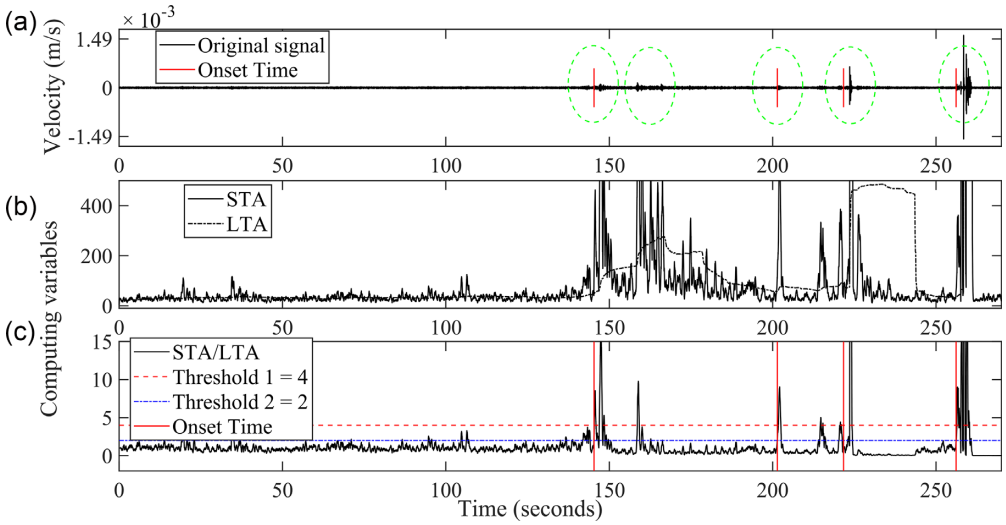

Figure 2. STA/LTA analysis results: (a) original signal where five events (circled in green) have been manually selected. Solid red lines are the event onset times detected by STA/LTA; (b) values of STA and LTA and (c) thresholds used as criteria for target event detection.

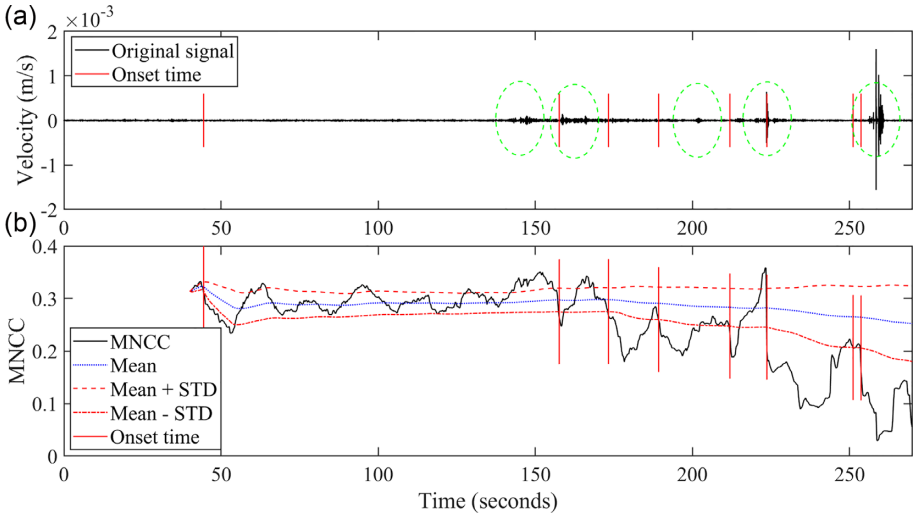

Figure 3. Cross-correlation detection (MNCC) results. (a) Original signal, where the five events (circled in green) have been manually selected. Solid red lines are the event onset times detected by MNCC and (b) analysis results, where the thresholds used to detect the events are represented.

identified even if they did not occur. In Fig. 3(b), the MNCC curve displays considerable variation, and it is easily disrupted by nearby events. For these reasons, it is suggested that MNCC is preferable for use in a stable monitoring environment (or with filtered signals and high signal-to-noise ratio data) or for single event detection, and therefore, it is not a suitable method for DESTRO, which operates with raw signals and in complicated environments.

Finally, in DESTRO, STA/LTA is chosen for single-component detection, and the process flowchart is shown in Fig. 4. In addition to the detected thresholds (*threshold 1* and *threshold 2* defined previously), a minimum event duration [*MINevent*, set equal to 0.4 s, i.e. equal to the short-time window (*STw*) in this study] and a minimum interval time [*MINinterval*, set equal to 14 s, i.e. equal to the long-time window (*LTw*)] between two events are defined to separate events. According to the monitoring site environment, the mean amplitude of ambient noise is $2 \times 10^{-5}\,\mathrm{m\,s^{-1}}$, and the seismic event detection ability is $4 \times 10^{-5}\,\mathrm{m\,s^{-1}}$, or sometimes smaller depending on the ambient noise and event duration.

3 EVENT-TYPE DEFINITION

In DESTRO, based on the characteristics of the frequency and amplitude, five seismic event types are defined: EQ, tremor (TR), RF, multispike event (MS) and subordinate MS (SMS) events, where the only difference between MS and SMS is the maximum frequency (F_m), set higher than 60 Hz and lower than 60 Hz, respectively. This difference is related to the material and the distance between the event source and receiver/s. The typical original signal traces and spectrograms of the five event types and those for the artificially released rockfall (ARF) are shown in Fig. 5. EQ (Fig. 5a) is identified as an easily detectable regional EQ, and the TR event (Fig. 5b) is a remote EQ or tectonic activity characterized by a long duration, low amplitude and low frequency due to the long distance of and energy attenuation during propagation. MS (Figs 5c and d) and RF (Figs 5e and f) are supposed rock cracking or small block falls and RFs, respectively, with a high frequency and short duration. For the purpose of RF classification, the discrimination between RF and MS is based on the maximum amplitude (A_m) threshold

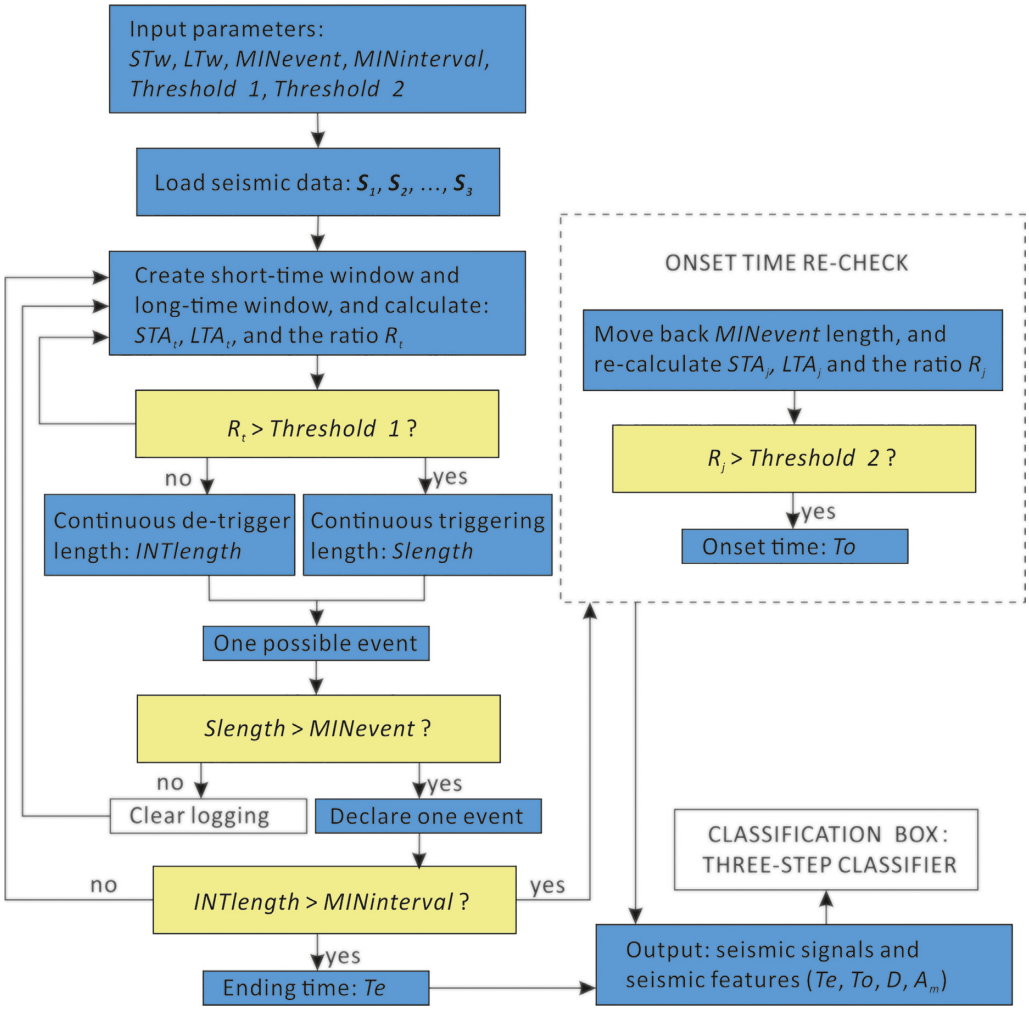

Figure 4. The flowchart of seismic event detection in DESTRO. In the flowchart, D and A_m are the duration and maximum amplitude of a detected event, respectively.

because their spectral attributes and waveform attributes look very similar. Unfortunately, this hypothesis of MS has not been validated until now (Arosio *et al.* 2009; Lenti *et al.* 2012; Lu *et al.* 2012, 2013).

To analyse the seismic features and feature weights, a seismic event-type training database is built. All the events in the database are manually picked from the east–west component of the traces recorded by station TOR 1 [see Fig. 1 and Lotti *et al.* (2018) or Feng *et al.* (2019) for its location within the quarry area] during a seismic monitoring window of 12 d, including the two days of the ARF test. The database contains 174 EQ events, 239 TR events, 90 ARFs, 75 natural rockfalls (NRF) manually selected based on the waveform, amplitude, duration, etc., and 1424 MS events (including SMS).

4 FEATURE DEFINITION

4.1 Methodology

To obtain good quality in seismic event classification, the choice of seismic features is critical, and it is important to keep the number of features as low as possible (Benitez *et al.* 2007; Vallejios and McKinnon 2013; Provost *et al.* 2017). In this study, nine seismic features are defined related to the event power (maximum amplitude A_m, energy density E_a and energy variation R_{ea}), spectrogram (maximum frequency F_m and frequency spectrum variation R_{fv}), waveform (number of peaks N_p), duration (D) and values at multiple stations (amplitude ratio R_a and frequency ratio R_f).

The frequency is one of the most important parameters of seismic signals and reflects the physical characteristics of the event source. The maximum frequency (F_m) is a frequency value with the maximum fast Fourier transform coefficient (FFTA, as defined in Feng *et al.* 2019) in the spectrogram (Daubechies 1992). This means that the signal of the F_m frequency band is the most powerful in the entire trace generated by the event. The maximum amplitude (A_m) is the maximum value of samples (x_i) in a time-series and represents the most powerful moment in the entire event duration. The calibrations of F_m and A_m are shown below.

$$F_m = i = \operatorname{argmax}(\mathrm{FFTA}_i), \tag{1}$$

$$A_m = \max(x_i), \tag{2}$$

To avoid the shortcomings associated with F_m, the frequency spectrum variation (R_{fv}) is newly introduced. It represents the energy distribution between the high-frequency bands [20–100 Hz] and low-frequency bands [3–16 Hz] and is calculated as the energy ratio

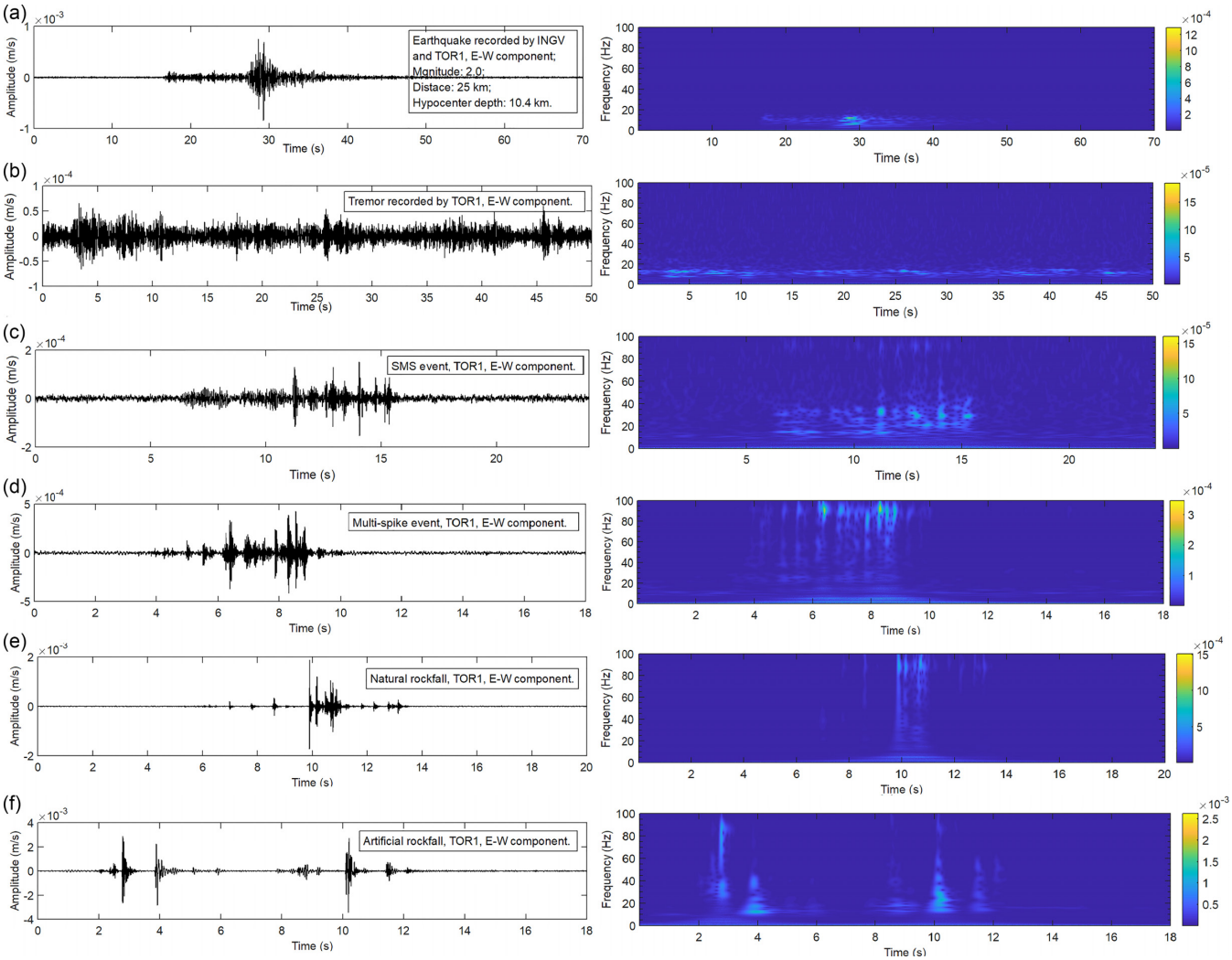

Figure 5. Original signal traces and time–frequency wavelet transforms of the five event types. TOR 1 is the name of one of the four seismic stations in the monitoring system (see Fig. 1 for its location). Moreover, the NRF in picture is not confirmed, but it has the same waveform (multiple spikes), duration, amplitude and high frequency as an ARF based on seismic analysis.

between the two frequency bands, as in eq. (3). The R_{fv} comparison of the five event types in Fig. 5 is shown in Fig. S11 (Supporting Information):

$$R_{fv} = \frac{\sum_{i=20}^{i=100} \mathrm{FFTA}_i^2}{\sum_{j=3}^{j=16} \mathrm{FFTA}_j^2}, \tag{3}$$

Seismic energy (E) is a relevant feature used to separate EQ events from TR events. In this study, it is calculated at each station and is defined as the integral of the squared seismic amplitude (A_m). It is important to note that given this definition, the employed energy is a relative quantity and not an absolute one because it is calculated at each station. Thus, factors such as attenuation effects and geometrical spreading are not included, and the chance of introducing processing errors is reduced (Dammeier *et al.* 2011). To decrease the duration effect in the energy calculation, a feature of the energy density (E_a) reflecting the energy density distributed over the entire event duration is proposed. The equations for E and E_a are shown in eqs (4) and (5):

$$E = \sum_{i=1}^{N} {x_i}^2, \tag{4}$$

$$E_a = \frac{E}{D}, \tag{5}$$

where N is the number of samples in a single detected event, D is the duration of one event and x_i is the velocity (signal amplitude) of sample i.

According to the observations of the ARF test and the generated signal traces, in RF and MS events, a large portion of the seismic energy is usually concentrated at the impact or cracking moment, while the energy of EQ and TR events is mostly distributed and varies over the entire event duration (Fig. 5). This phenomenon is especially clear for RF events. Therefore, energy variation (R_{ea}) could be efficiently used to distinguish RF events from EQ events. R_{ea} is defined as E_a divided by the square of A_m and indicates the degree of energy concentration, as shown in eq. (6).

$$R_{ea} = \frac{E_a}{{A_m}^2}, \tag{6}$$

The amplitude ratio (R_a), defined in eq. (7), is the ratio of A_m between two different seismic stations TOR i and TOR j,

where $A_{mi} >= A_{mj}$:

$$R_a = \frac{A_{mi}}{A_{mj}}, \tag{7}$$

Consequently, as defined in eq. (8), the frequency ratio (R_f) is the ratio of F_m between two different seismic stations TOR i and TOR j, where $F_{mi} >= F_{mj}$:

$$R_f = \frac{F_{mi}}{F_{mj}}, \tag{8}$$

R_a and R_f are first proposed in this study, and they are very important features for DESTRO to classify remote and local events. For example, the values of A_m and F_m for some seismic events that occur far from the seismic network are often similar at different stations, so both the R_a and R_f values are close to 1. The part of the energy characterized by high frequencies is attenuated or filtered during long-distance propagation. In contrast, the values of R_a and R_f for events that occur near the seismic network or inside it (such as a local RF or crack breaking) are very high because the relative distances between stations and sources are proportionally different and the attenuations are different. In terms of this relationship, the features of R_a and R_f can be used to efficiently separate remote events and local events.

The waveform peaks (N_p) have been defined as the number of periods (peaks) exceeding a threshold calculated on the basis of the amplitude standard deviation (computed in a 0.4 s-long sliding window, see also Feng *et al.* 2019). Although N_p is significantly influenced by many factors, such as the geomorphology, seismic energy and threshold chosen for detection, it clearly discriminates between EQs (which typically have a single peak) and RFs (which have as many peaks as the number of rebounds of the rock on the ground, Fig. 5). For TR and MS events, the signal amplitudes are too small to detect waveform peaks with the same threshold as applied for EQs and RFs, so in this study, N_p is only used in EQ and RF classification.

Duration is another very important complementary feature for seismic event classification, even though it highly depends on specific topographical conditions, the event source location and the attenuation in propagation as waveform peaks. In this study, the duration of an event was defined as the time elapsed from the first sample triggered by the threshold of STA/LTA = 2 (for more information on the seismic event detection method for STA/LTA, see Allen 1978; Trnkoczy 1998) to the last sample triggered by the threshold of STA/LTA = 4. The calculated duration, given the principle of the STA/LTA detection method, is shorter than the real duration. One example of the duration of an ARF is plotted in Fig. S12 in the Supporting Information.

4.2 More discussion on seismic features

In this study, five key features (F_m, R_{fv}, A_m, R_f and R_a) and four complementary features (E_a, D, R_{ea} and N_p) were defined for event classification. In particular, multistation attributes (R_f and R_a) and frequency variations (R_{fv}) were proposed for the first time. Accordingly, the distribution in the database event classes of all the features are analysed in detail in the Supporting Information. These features are useful for seismic event classification and initial feature weight computing (see Section 5.1). Considering the spectral attributes, seismic events can be classified into high-frequency events (RF and MS) and low-frequency events (EQ and TR), while considering the event-power attributes, the events can be classified into powerful events (EQ and RF) and weak events (TR and MS). Multistation attributes are thus applied to classify events as local (MS and RF) and remote (EQ and TR) events. The waveform peaks and durations allow for the precise distinction between EQs and RFs and between EQs and TRs, respectively. Consequently, most of these features extracted from signal traces are successfully applied, except for the waveform peaks and durations. In fact, (i) it is difficult to precisely pick in an automatic way the end time of an event, even though the lengths of triggered samples are applied instead of the true durations, and (ii) the computation of the waveform peaks is still ineffective due to the need for amplitude threshold selection and the strong variation in the amplitudes of different events. In general, the five key features performed very well, but the four complementary features should be improved to find a more relevant relationship with amplitude. Additionally, more seismic event samples and monitoring cases need to be studied.

5 CLASSIFIER DESIGN

In this study, a three-step classifier is designed based on the seismic features and information from multiple stations in a monitoring array. The seismic features, as discussed in Section 4, include five key features (F_m, R_{fv}, A_m, R_f and R_a) that play a determinant role, and four complementary features (E_a, D, R_{ea} and N_p) that support precise classification. Three different classifiers are designed in the three-step classifier. The first classifier (classifier S) is designed as a single-component classifier. The second classifier (classifier C) is proposed as a multicomponent classifier, that is at one seismic station, multicomponent event integration and re-classification are performed, based on the results of classifier S of the three components. The third classifier (classifier M) performs site-event integration and event-type reclassification considering the results of classifier C for the entire monitoring network. The full classification flowchart is shown in Fig. 6. In this study, as shown in Fig. 1, the monitoring network is comprised of four seismic stations, and each station has three components, E–W, N–S and vertical Z components. Furthermore, in addition to the five event types, namely, EQ, TR, SMS, MS and RF defined above, another event type, unknown events (UNs), is defined. UNs consist of MS events with $F_m < 3$ Hz or $A_m > 1$ m s^{-1} and EQ or TR events recognized by only a single component.

5.1 Single-component classifier design (classifier S)

To perform single-component classification, a different weight is assigned to each feature (key and complementary) . The initial weights are calculated from the distribution of seismic features in the database, and then they are modified with a manual calibration process considering the bias in the data because some event types could be over- or under-represented. An example of the initial weight computation of EQ (W_{EQfm1}) in the range of F_m (0–3 Hz) is shown in the Supporting Information, and the initial and modified weights of nine seismic features in the training set are computed in Tables S1–S3 (Supporting Information). As soon as the modified weights (W') of the nine features are assigned, each feature is extracted with a weight array (**W**) that represents the six event-type occurrence rates in each range of each feature. Next, all the weight arrays from the nine features are multiplied by multiplying corresponding

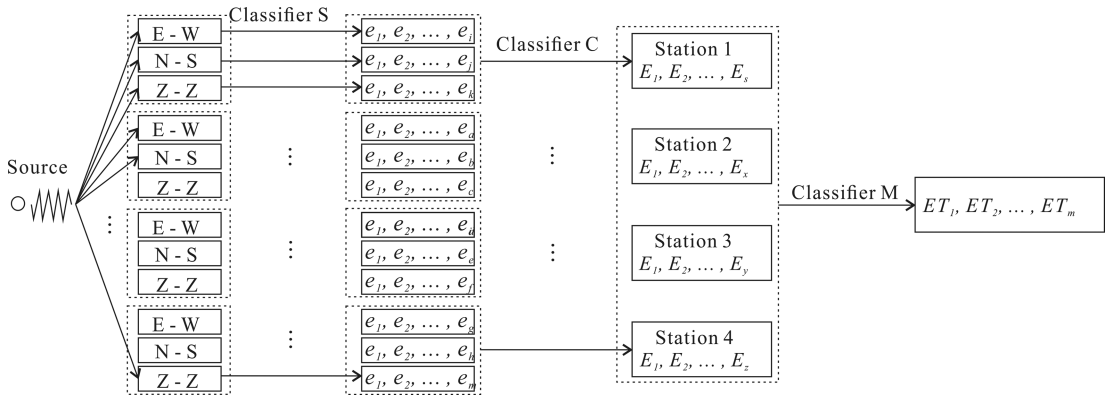

Figure 6. Seismic event classification flowchart in DESTRO. e_i, E_i and ET_i are the event types as classified by classifiers S, C and M, respectively.

elements to obtain a final product array (**V**) that represents the final occurrence rate of each event type (eqs 9 and 10).

$$\mathbf{W}_{fm} = \left[\boldsymbol{W'}_{eqfm}, \boldsymbol{W'}_{trfm}, \boldsymbol{W'}_{smsfm}, \boldsymbol{W'}_{msfm}, \boldsymbol{W'}_{rffm}, \boldsymbol{W'}_{unfm}\right], \tag{9}$$

$$\mathbf{V} = \mathbf{W}_{fm} .*\mathbf{W}_{rfv}.*\mathbf{W}_{am}.*\mathbf{W}_{rf}.*\mathbf{W}_{ra}.*\mathbf{W}_{ea}.*\mathbf{W}_{d}.*\mathbf{W}_{rea}.*\mathbf{W}_{np} = \left[\boldsymbol{V}_{eq}, \boldsymbol{V}_{tr}, \boldsymbol{V}_{sms}, \boldsymbol{V}_{ms}, \boldsymbol{V}_{rf}, \boldsymbol{V}_{un}\right], \tag{10}$$

where W'_{eqfm}, W'_{trfm}, W'_{smsfm}, W'_{msfm}, W'_{rffm} and W'_{unfm} are the modified weights of EQ, TR, SMS, MS, RF and UN, respectively; the variables $\mathbf{W}_{\mathrm{fm}}$, $\mathbf{W}_{\mathrm{rfv}}$, $\mathbf{W}_{\mathrm{am}}$, $\mathbf{W}_{\mathrm{rf}}$, $\mathbf{W}_{\mathrm{ra}}$, $\mathbf{W}_{\mathrm{ea}}$, $\mathbf{W}_{\mathrm{d}}$, $\mathbf{W}_{\mathrm{rea}}$ and $\mathbf{W}_{\mathrm{np}}$ are the weight arrays of the seismic features F_m, R_{fv}, A_m, R_f, R_a, E_a, D, R_{ea} and N_p, respectively.

Finally, each event type is assigned an ID number (e.g. events EQ, TR, SMS, MS, RF and UN are represented by 1, 2, 3, 4, 5 and 7, respectively) and the maximum element in the final matrix **V** represents the event type (e_i) classified by classifier S.

5.2 Multicomponent classification (classifier C)

Classifier C is designed to classify event types (E_1, E_2, . . . , E_s) at a single station by integrating and reclassifying the events identified for each of the three components at one station. The process flowchart for classifier C is shown in Fig. S9 (Supporting Information). The main process can be divided into three phases. First, all of the event parameters, such as the onset time (*To*), end time (*Te*), event type (e_i) and detected component number, are marked as input parameters. Second, all the events from the three components with the respective features are integrated into one event series and sorted in the time domain, and a judgement for event integration and the reclassification of specific integrated events is performed. Finally, events from three components are reclassified according to the reclassification criteria to obtain a station-event series (E_1, E_2, . . . , E_s) with event types and seismic features. The details of the integrated judgement and reclassification criteria are shown in the Supporting Information.

5.3 Multistation classification (classifier M)

Classifier M is designed to integrate all the events from the seismic network. In addition to the EQ, TR, SMS, MS, RF and UN even types, classifier M introduces a secondary specification to characterize their influence (classified as a regional event, slope-scale event, local event, very local event, or point event; Table 1) by multiplying the event-type ID number by a power of 10 (from 10^3 to 10^{-1}). The events are therefore classified as a site-event series (ET_1, ET_2, . . . , ET_m) based on both the event type and scale.

In classifier M, the processing steps are divided into three phases (as shown in Fig. S10, Supporting Information): data preparation, event integration and event-type reclassification. The first and second parts are the same as those for classifier C; in the third part, the number of stations that detect the same event is determined (s equals 1, 2, 3 or 4), and the secondary specification is obtained. The event-type reclassification criteria for classifier M and the detailed secondary event-type definitions are provided in the Supporting Information.

6 DESTRO PERFORMANCE

Based on the algorithms proposed and implemented in MATLAB 2017b, a Graphical User Interface was designed to combine seismic event detection, classification and event spectrogram rechecking. DESTRO is specially designed for RF hazard monitoring combined with EQ detection. As processing outputs, the event types, onset times and nine seismic features are provided.

6.1 DESTRO detection accuracy

To evaluate the detection accuracy, a test signal of 55 min that recorded 30 different events was chosen among the entire seven-month monitoring data set (the original signal is shown in Fig. S13, Supporting Information). The DESTRO code managed to automatically detect all 30 events.

The onset times automatically detected by DESTRO (t_D) and the onset times manually picked (t_m) are shown in Table 2, together with all the errors between t_D and t_m (calculated as t_D—t_m). It can be noted that (1) only one error is larger than one second, and most of the others errors are near zero; (2) all of the errors are larger than 0, which means that for the onset time selection method, STA/LTA, there is a lag based on the length of the selected sliding window and (3) the mean error is 0.2178 s, which is treated as the median lag. The results also show that there were no missing or fake events.

6.2 Training set evaluation

To evaluate the DESTRO classification performance in the database, a test is performed on a continuous monitoring trace of 12 d, from

Table 1. The identification numbers (ID numbers) of the event categories (event type and scale). Note that signals primarily classified as EQs or TRs but detected by only one component or one station are instead classified as UN.

Event types		Scales				
		Regional (R)	Slope-scale (S)	Local (L)	Very Local (vL)	Point (P)
EQ	1	1000	100	10	7 (UN)	7 (UN)
TR	2	2000	200	20	7 (UN)	7 (UN)
SMS	3	3000	300	30	3	0.3
MS	4	4000	400	40	4	0.4
RF	5	5000	500	50	5	0.5
UN	7	7000	700	70	7	7

Table 2. The onset times picked manually and by DESTRO with the corresponding errors.

Event number	Manual onset times (s)	DESTRO onset times (s)	Errors (s)	Events Number	Manual onset times (s)	DESTRO onset times (s)	Errors (s)
1	374.4	374.52	0.12	16	1956.13	1956.16	0.03
2	466.71	466.75	0.04	17	2027.96	2028.025	0.065
3	522.825	522.86	0.035	18	2091.85	2092.01	0.16
4	538.25	538.345	0.095	19	2261.65	2261.95	0.3
5	577.23	577.87	0.64	20	2480.48	2480.505	0.025
6	649.01	649.05	0.04	21	2572.54	2572.64	0.1
7	772.8	773.205	0.405	22	2828.15	2828.3	0.15
8	796.38	796.685	0.305	23	2941.05	2941.565	0.515
9	1039.03	1039.11	0.08	24	3060.16	3060.23	0.07
10	1143.05	1143.185	0.135	25	3174.31	3174.355	0.045
11	1218.95	1219.015	0.065	26	3221.02	3222.235	1.215
12	1328.78	1329.145	0.365	27	3267.33	3267.445	0.115
13	1502.925	1502.96	0.035	28	3322.25	3322.28	0.03
14	1582.93	1582.945	0.015	29	3392.7	3392.795	0.095
15	1769	1769.44	0.44	30	3409.33	3410.145	0.815

2012 December 7 to 18, that includes all the events in the training database. In total, 471 EQ events, 194 TR events, 2819 SMS events, 3683 MS events and 318 RF events were classified by DESTRO. The DESTRO classification results are then compared with manual classification results for the same period, and results are plotted in Fig. 7. The following observations can be done: (i) 96 per cent of the EQ events and 100 per cent of the RF events in the training database are correctly classified by DESTRO; (ii) 4 per cent of the EQ events (six EQ events) are still not classified correctly by DESTRO; specifically, three EQ events were classified in the TR category, one as an SMS, and two as RFs; (iii) 99.5 per cent of SMS and MS events were classified successfully, and only 0.5 per cent of MS events (seven MS events) were classified incorrectly, that is, four events classified as EQ, two as UN, and one as TR and (iv) many TR events were incorrectly classified as UN, SMS, or MS events.

In summary, from the accuracy evaluation results, 100 per cent of the event categories of RF, and 99.5 per cent SMS plus MS were successfully classified and separated from the all-around noise. With respect to the strict classification criteria of EQs and TRs, some EQ and TR events were incorrectly classified as UN, and some EQs were classified as TRs when the energy of an EQ was too low to be detected by more than two stations. For the reasons that follow, there are still two EQ events classified as RFs: (i) in one case, the EQ event merged with too many other high-frequency events, which contributed to a high R_{fv} value, and (ii) for the other EQ events, the maximum frequency is higher than the F_m threshold (20 Hz) used in the classification of EQs.

6.3 Earthquake classification

To evaluate the DESTRO classification performance of EQs, a longer monitoring data set of 25 d (2012 December 7–31) recorded at Torgiovannetto is selected. All the EQ and TR events detected by DESTRO (984 EQ and 370 TR) are compared with the events from the INGV EQ database (573 EQs that occurred in the same period within a radius of less than 300 km). The result of this comparison is shown in Fig. 8. 58.8 per cent of the EQs recorded by INGV are also clearly recognized by DESTRO, simply from an onset time comparison, but 41.2 per cent of the EQs were not confirmed in DESTRO.

To determine why 41.2 per cent of the EQs are unconfirmed in DESTRO, the magnitudes and epicentre distances are analysed. The distance versus magnitude result is shown in Fig. 9. In particular, blue dots are the EQs confirmed as EQs by DESTRO, and the yellow dots are EQs only recorded by INGV. The histogram shows the percentages of confirmed and unconfirmed EQs in two distance ranges: less than 100 km and from 100 to 300 km. The EQ distances recorded by INGV ranged from 4.4 to 292 km, and the magnitudes ranged from 0.4 to 3.2. From the results, almost 64.9 per cent of the EQs with epicentre distances less than 100 km are confirmed by DESTRO, and in the distance range of 100–300 km, only 21.3 per cent are confirmed. This result is because the EQs that occurred nearby are more easily confirmed with a small onset time delay and attenuation than EQs that occurred farther away with strong attenuation that are difficult to detect with DESTRO or cannot be simply confirmed with onset times because

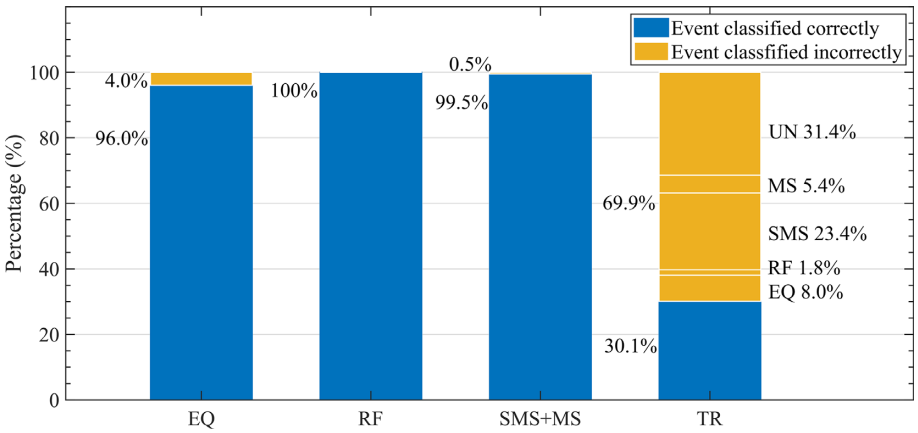

Figure 7. The classification results of DESTRO for the 12-d monitoring data set.

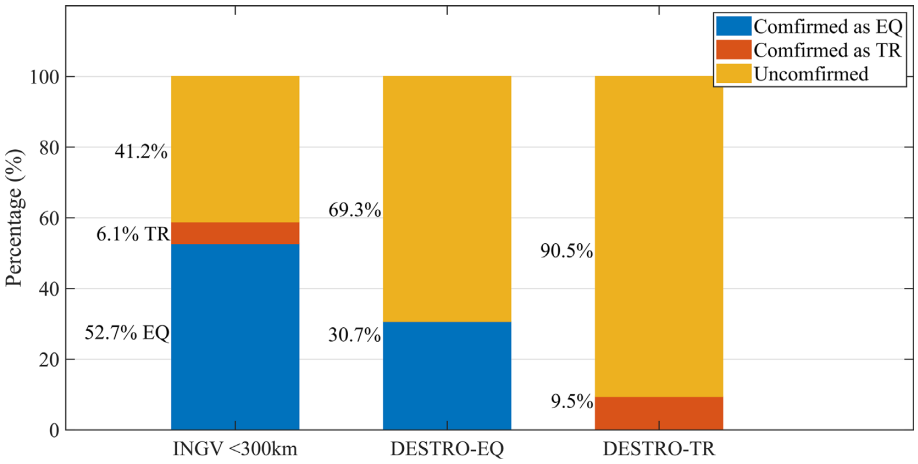

Figure 8. The detection results for EQs and TRs in DESTRO and a comparison with the INGV EQ database from 2012 December 7 to 31 based only on the onset time.

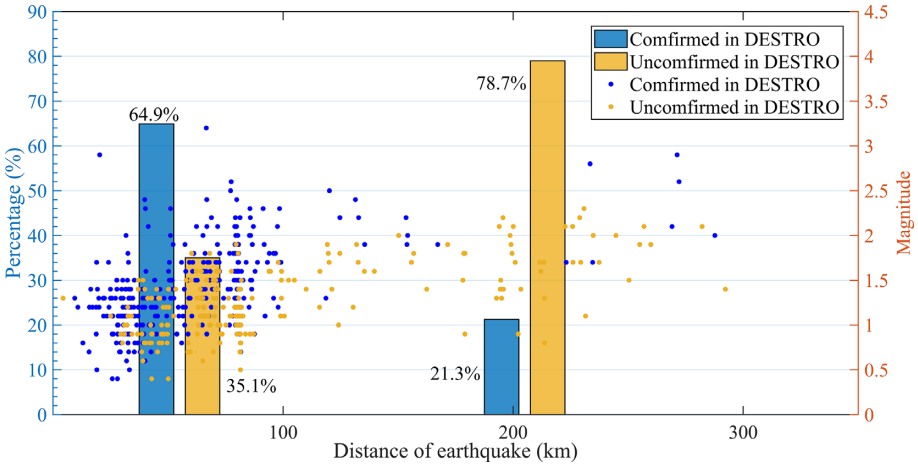

Figure 9. The distances and magnitudes of EQs recorded in the INGV EQ database that were less than 300 km during the period 2012 December 7–31.

of large onset time delays. Moreover, high EQ magnitudes are easier to detect by DESTRO than low magnitudes, as validated in Fig. 9.

In summary, the reasons why 41.2 per cent of EQs were not confirmed in DESTRO are as follows: (i) the onset time delay makes it difficult to track EQs from INGV to DESTRO since some EQ epicentres were distant from the stations and signal were influenced by high attenuation; (ii) a low-magnitude EQ is not a single event but usually occurs with a series of post-shocks, so there will be some differences in post-shock recordings between the seismic network and INGV; (iii) the intrinsic drawbacks of this monitoring network (the stations are located at a distance of 200 m), that is a very small network scale, compared with the scale of the national EQ monitoring network, so some EQs could be merged into one

TR event. Moreover, classification errors can occur in DESTRO. For example, (i) some EQs could be classified as TR events since the definitions of TRs and EQs are similar (differences related to duration and energy attributes); (ii) some EQs could be classified as UN events, since EQ and TR events should be detected by more than two stations, otherwise an event will be classified as UN; and (iii) some EQs may be classified as SMS, MS or RF events when EQ events merge with SMS, MS, or RF events since high-frequency events are prioritized and kept in DESTRO.

6.4 Artificially released rockfall classification

To evaluate the capability of DESTRO in RF detection, a continuous monitoring period of 4 hr and 40 min that covers an ARF test (Feng *et al.* 2019) is analysed. A total of 109 RFs were detected. Of the 90 ARFs, 88 ARFs were classified correctly by DESTRO, and 2 ARFs were classified as SMS events (because their amplitudes were less than the 0.001 m s^{-1} threshold defined). The hit rate of DESTRO in this test is 100 per cent. On the other hand, 21 events in excess were detected, for a total of 109 signals classified as RFs. Even a manual check on these 21 extra signals made it impossible to distinguish them from the verified RFs, since they probably represent actual involuntary RFs caused by the passage of the experiment operators or even small unnoticed NRFs. This means that the confidence against false negatives (i.e. of detecting real RFs from raw seismic data) is $\geq$ 81 per cent (where 81 per cent represents the assumption that the 21 extra events detected were all errors).

7 CONCLUSIONS

After comparing the differences and performances of the STA/LTA method and cross-correlation method, the most traditional and widely used STA/LTA method was chosen in DESTRO because of (i) the processing stability with raw monitoring data, (ii) the flexible parameters and (iii) good performance in event detection and onset time selection. Nevertheless, the STA/LTA method struggles to separate different events and defines the ends of two nearly coincidental events, even though the minimum event duration and minimum interval time were defined as two extra parameters. To classify the events by integrating all the signal trace features from multiple components and stations, nine seismic features and a three-steps classifier (includes classifiers S, C and M) are designed and implemented in coordination. Classifier S integrates the seismic feature matrices over time and classifies each component based on the initial event types. Then, classifier C integrates all the events detected in the three components of one station and reclassifies them into primary event types. Finally, classifier M, by introducing a secondary specification that describes the scale of influence, integrates all the events detected by the monitoring network and obtains a final site-event series with event types, scales and seismic characteristics.

Considering the performance of DESTRO in classification, there are 96 per cent EQ and 100 per cent RF events in the monitoring period of 12 d. Based on a training database of correctly classified EQs, 58.8 per cent of EQs have distances less than 300 km (64.9 per cent of EQs have distances less than 100 km) in 25 d that were clearly identified by both INGV and DESTRO, simply from an onset time comparison. In the 4.7-hr monitoring time period, which includes the artificial RF release test, 80.7 per cent of RFs were correctly classified (assuming that the extra detected events were all errors), and 1.8 per cent were classified as SMS.

In addition to use DESTRO in detection and classifier design, more studies should be performed on the following topics: (i) six event types (EQ, TR, SMS, MS, RF and UN) are defined in DESTRO, but only EQ and RF are confirmed by both the INGV database and the ARF test respectively, and MS and SMS, representing rock cracking or tiny block falls, were not confirmed in the laboratory or with field testing (Senfaute *et al.* 2009; Lu *et al.* 2012, 2013; Coviello *et al.* 2015); (ii) the weights of features for classifier S were modified from the distribution of seismic features in the training database, and the training database is not sufficiently relevant and has some bias; therefore, a more relevant and larger database or more cases should be used in the future. DESTRO is especially applied in rock slope seismic monitoring combines with EQ monitoring. This approach is useful for rock mass dynamic state monitoring, not only for the surface but also for the subsurface, even in slope instability forecasting and risk evaluation, once the signal of rock cracking is checked in the laboratory and field tests. Moreover, since DESTRO can separate the event types of EQ and RF, the method would also be useful in defining the relationship between RFs and EQs with the meteorological events in EQ-prone areas.

ACKNOWLEDGEMENTS

University of Florence, Department of Earth Sciences (Italy) supported this research as part of its programme to improve rockslide early warning systems (PRIN 2009–Advanced monitoring techniques for the development of early warning procedures on large rockslides—prot. 20084FAHR7_001). We gratefully acknowledge Sara Electronic Instrument for providing the devices installed at the four seismic stations. We thank Massimiliano Nocentini and Luca Lombardi (Unifi-DST) for the extensive efforts installing and maintaining the network and making the microseismic data available. We also thank Alessia Lotti (Unifi-DST) for providing us with the entire seismic monitoring data set acquired for her Ph.D. work. We also acknowledge the MATLAB support from Dr Lin Gao (Unifi-DINFO). Finally, the financial support provided by Prof Nicola Casagli and the China Scholarship Council (CSC) to Liang Feng during his study abroad in Italy is acknowledged.

REFERENCES

Akhouayri, E.S., Agliz, D. & Atmani, A., 2014. Automatic detection and picking of P-wave arrival in locally stationary noise using cross-correlation, *Digit. Signal Process.,* **26,** 87–100.

Akhouayri, E.S., Agliz, D., Zonta, D. & Atmani, A., 2015. A fuzzy expert system for automatic seismic signal classification, *Expert Syst. Appl.,* **42**(3), 1013–1027.

Akram, J. & Eaton, D.W., 2016. Refinement of arrival-time picks using a cross-correlation based workflow, *J. appl. Geophys.,* **135,** 55–66.

Allen, R.V., 1978. Automatic earthquake recognition and timing from single traces, *Bull. seism. Soc. Am.,* **68**(5), 1521–1532.

Allen, R., 1982. Automatic phase pickers: their present use and future prospects, *Bull. seism. Soc. Am.,* **72**(6B), S225–S242.

Arosio, D., Longoni, L., Papini, M., Scaioni, M., Zanzi, L. & Alba, M., 2009. Towards rockfall forecasting through observing deformations and listening to microseismic emissions, *Nat. Hazards Earth Syst. Sci.,* **9**(4), 1119–1131.

Arosio, D., Longoni, L., Papini, M., Boccolari, M. & Zanzi, L., 2018. Analysis of microseismic signals collected on an unstable rock face in the Italian Prealps, *Geophys. J. Int.,* **213**(1), 475–488.

Bendat, J.S. & Piersol, A.G., 2011. Random data: analysis and measurement procedure, *sect. 11.4*. John Wiley & Sons.

Benítez, M.C., Ramírez, J., Segura, J.C., Ibanez, J.M., Almendros, J., García-Yeguas, A. & Cortes, G., 2007. Continuous HMM-based seismic-event

classification at Deception Island, Antarctica, *IEEE Trans. Geosci. Remote Sens.,* **45**(1), 138–146.

Burtin, A., Hovius, N., McArdell, B.W., Turowski, J.M. & Vergne, J., 2014. Seismic constraints on dynamic links between geomorphic processes and routing of sediment in a steep mountain catchment, *Earth Surf. Dyn.,* **2**(1), 21–33.

Coviello, V., Chiarle, M., Arattano, M., Pogliotti, P. & di Cella, U.M., 2015. Monitoring rock wall temperatures and microseismic activity for slope stability investigation at JA Carrel hut, Matterhorn, in *Engineering Geology for Society and Territory-Volume 1,* pp. 305–309, Springer, Cham. doi:10.1007/978-3-319-09300-0_57.

Coviello, V., Arattano, M., Comiti, F., Macconi, P. & Marchi, L., 2019. Seismic characterization of debris flows: insights into energy radiation and implications for warning, *J. geophys. Res.: Earth Surf,* **124**(6), 1440–1463.

Curilem, G., Vergara, J., Fuentealba, G., Acuña, G. & Chacón, M., 2009. Classification of seismic signals at Villarrica volcano (Chile) using neural networks and genetic algorithms, *J. Volc. Geotherm. Res.,* **180**(1), 1–8.

Dammeier, F., Moore, J.R., Haslinger, F. & Loew, S., 2011. Characterization of alpine rockslides using statistical analysis of seismic signals, *J. geophys. Res.: Earth Surf.,* **116**(F4), doi:10.1029/2011JF002037.

Dammeier, F., Moore, J.R., Hammer, C., Haslinger, F. & Loew, S., 2016. Automatic detection of alpine rockslides in continuous seismic data using hidden Markov models, *J. geophys. Res.: Earth Surf.,* **121**(2), 351–371.

Fan, W., McGuire, J.J., de Groot-Hedlin, C.D., Hedlin, M.A.H., Coats, S. & Fiedler, W., 2019. Stormquakes, *Geophys. Res. Lett.,* doi:10.1029/2019GL084217.

Daubechies, I., 1992. *Ten Lectures on Wavelets,* Society for Industrial and Applied Mathematics, p. 357.

Feng, Z., 2011. The seismic signatures of the 2009 Shiaolin landslide in Taiwan, *Nat. Hazards Earth Syst. Sci.,* **11,** 1559–1569.

Feng, L., Pazzi, V., Intrieri, E., Gracchi, T. & Gigli, G., 2019. Rockfall seismic features analysis based on in situ tests: frequency, amplitude, and duration, *J. Mt. Sci.,* **16**(5), 955–970.

Feng, L. *et al.*, 2020. Rockfall localization from seismic polarization considering multiple triaxial geophones and frequency bands, *J. Mt. Sci.,* **17(7),** doi:10.1007/s11629-020-6132-1.

Froude, M.J. & Petley, D., 2018. Global fatal landslide occurrence from 2004 to 2016, *Nat. Hazards Earth Syst. Sci.,* **18,** 2161–2181.

Gibbons, S.J., Ringdal, F. & Kværna, T., 2012. Ratio-to-moving-average seismograms: a strategy for improving correlation detector performance, *Geophys. J. Int.,* **190**(1), 511–521.

Gracchi, T., Lotti, A., Saccorotti, G., Lombardi, L., Nocentini, M., Mugnai, F. & Fiaschi, A., 2017. A method for locating rockfall impacts using signals recorded by a microseismic network, *Geoenviron. Disasters,* **4**(1), 26. doi:10.1186/s40677-017-0091-z.

Guinau, M., Tapia, M., Pérez-Guillén, C., Suriñach, E., Roig, P., Khazaradze, G. & Echeverria, A., 2019. Remote sensing and seismic data integration for the characterization of a rock slide and an artificially triggered rock fall, *Eng. Geol.,* **257,** 105113. doi:10.1016/j.enggeo.2019.04.010.

Hafez, A.G., Khan, T.A. & Kohda, T., 2009. Earthquake onset detection using spectro-ratio on multi-threshold time–frequency sub-band, *Digit. Signal Process.,* **19**(1), 118–126.

Hafez, A.G., Khan, M.T.A. & Kohda, T., 2010. Clear P-wave arrival of weak events and automatic onset determination using wavelet filter banks, *Digit. Signal Process.,* **20**(3), 715–723.

Heck, M., Hammer, C., Herwijnen, A.V., Schweizer, J. & Fäh, D., 2018. Automatic detection of snow avalanches in continuous seismic data using hidden Markov models, *Nat. Hazards Earth Syst. Sci.,* **18**(1), 383–396.

Helmstetter, A. & Garambois, S., 2010. Seismic monitoring of Séchilienne rockslide (French Alps): analysis of seismic signals and their correlation with rainfalls, *J. geophys. Res.: Earth Surf.,* **115**(F3), doi:10.1029/2009JF001532.

Hibert, C., Mangeney, A., Grandjean, G. & Shapiro, N., 2011. Slope instabilities in Dolomieu crater, Reunion Island: From seismic signals to rockfall characteristics, *J. geophys. Res.,* **116,** F04032, doi:10.1029/2011JF002038.

Hibert, C., Mangeney, A., Grandjean, G., Baillard, C., Rivet, D., Shapiro, N.M. & Crawford, W., 2014. Automated identification, location, and volume estimation of rockfalls at Piton de la Fournaise volcano, *J. geophys. Res.: Earth Surf.,* **119**(5), 1082–1105.

Hibert, C., Malet, J.P., Bourrier, F., Provost, F., Berger, F., Bornemann, P. & Mermin, E., 2017. Single-block rockfall dynamics inferred from seismic signal analysis, *Earth Surf. Dyn.,* **5**(2), 283, doi:10.5194/esurf-5-283-2017.

Hungr, O., Leroueil, S. & Picarelli, L., 2014. The Varnes classification of landslide types, an update, *Landslides,* **11**(2), 167–194.

Kortström, J., Uski, M. & Tiira, T., 2016. Automatic classification of seismic events within a regional seismograph network, *Comput. Geosci.,* **87,** 22–30.

Küperkoch, L., Meier, T., Lee, J. & Friederich, W. EGELADOS Working Group., 2010. Automated determination of P-phase arrival times at regional and local distances using higher order statistics, *Geophys. J. Int.,* **181**(2), 1159–1170.

Rocca, La, M., Galluzzo, D., Saccorotti, G., Tinti, S., Cimini, B., G. & Del Pezzo, E., 2004. Seismic signals associated with landslides and with a tsunami at Stromboli volcano, Italy, *Bull. seism. Soc. Am.,* **94**(5), 1850–1867.

Li, Z.Y., Huang, X.H., Yu, D., Su, J.R. & Xu, Q., 2019. Broadband-seismic analysis of a massive landslide in southwestern China: dynamics and fragmentation implications, *Geomorphology,* **336,** 31–39.

Lin, C.H., Kumagai, H., Ando, M. & Shin, T.C., 2010. Detection of landslides and submarine slumps using broadband seismic networks, *Geophys. Res. Lett.,* **37,** L22309, doi:10.1029/2010GL044685.

Lenti, L., Martino, S., Paciello, A., Prestininzi, A. & Rivellino, S., 2012. Microseismicity within a karstified rock mass due to cracks and collapses as a tool for risk management, *Nat. Hazards,* **64**(1), 359–379.

Lotti, A., Saccorotti, G., Fiaschi, A., Matassoni, L., Gigli, G., Pazzi, V. & Casagli, N., 2015. Seismic monitoring of rockslide: the Torgiovannetto quarry (Central Apennines, Italy), in *Engineering Geology for Society and Territory,* vol. **2,** pp. 1537–1540, eds. Lollino, G. *et al.*, Springer International Publishing, Switzerland, doi:10.1007/978-3-319-09057-3_272.

Lotti, A., Pazzi, V., Saccorotti, G., Fiaschi, A., Matassoni, L. & Gigli, G., 2018. HVSR analysis of rockslide seismic signals to assess the subsoil conditions and the site seismic response, *Int. J. Geophys,* article ID: 9383189, doi:10.1155/2018/9383189.

Lu, C.P., Dou, L.M., Liu, B., Xie, Y.S. & Liu, H.S., 2012. Microseismic low-frequency precursor effect of bursting failure of coal and rock, *J. appl. Geophys.,* **79,** 55–63.

Lu, C.P., Dou, L.M., Zhang, N., Xue, J.H., Wang, X.N., Liu, H. & Zhang, J.W., 2013. Microseismic frequency-spectrum evolutionary rule of rockburst triggered by roof fall, *Int. J. Rock Mech. Min. Sci.,* **64,** 6–16.

Manconi, A., Picozzi, M., Coviello, V., De Santis, F. & Elia, L., 2016. Real-time detection, location, and characterization of rockslides using broadband regional seismic networks, *Geophys. Res. Lett.,* **43**(13), 6960–6967.

Matsuoka, N., 2019. A multi-method monitoring of timing, magnitude and origin of rockfall activity in the Japanese Alps, *Geomorphology,* **336,** 65–76.

Panagiotakis, C., Kokinou, E. & Vallianatos, F., 2008. Automatic P-phase picking based on local-maxima distribution, *IEEE Trans. Geosci. Remote Sens.,* **46**(8), 2280–2287.

Pazzi, V., Morelli, S. & Fanti, R., 2019. A review of the advantages and limitations of geophysical investigations in landslide studies, *Int. J. Geophys.*, article ID: 2983087, doi:10.1155/2019/2983087.

Picotti, S., Francese, R., Giorgi, M., Pettenati, F. & Carcione, J.M., 2017. Estimation of glacier thicknesses and basal properties using the horizontal-to-vertical component spectral ratio (HVSR) technique from passive seismic data, *J. Glaciol.,* **63**(238), 229–248.

Provost, F., Hibert, C. & Malet, J.P., 2017. Automatic classification of endogenous landslide seismicity using the Random Forest supervised classifier, *Geophys. Res. Lett.,* **44**(1), 113–120.

Rabiner, L.R., 1989. A tutorial on hidden Markov models and selected applications in speech recognition, *Proc. IEEE,* **77**(2), 257–286.

Rodriguez, I.V., 2011. Automatic time-picking of microseismic data combining STA/LTA and the stationary discrete wavelet transform. *CSPG CSEG CWLS Convention, Convention Abstracts,* (1), 2–5.

Romeo, G., 1994. Seismic signals detection and classification using artiricial neural networks, *Ann. Geophys.,* **37**(3), doi:10.4401 /ag-4211.

Scarpetta, S., Giudicepietro, F., Ezin, E.C., Petrosino, S., Del Pezzo, E., Martini, M. & Marinaro, M., 2005. Automatic classification of seismic signals at Mt. Vesuvius volcano, Italy, using neural networks, *Bull. seism. Soc. Am.,* **95**(1), 185–196.

Senfaute, G., Duperret, A. & Lawrence, J.A., 2009. Micro-seismic precursory cracks prior to rock-fall on coastal chalk cliffs: a case study at Mesnil-Val, Normandie, NW France, *Nat. Hazards Earth Syst. Sci.,* **9**(5), 1625–1641.

Trnkoczy, A., 1998. Understanding & setting sta/lta trigger algorithm parameters for the k2, *Appl. Note,* **41,** 16–20.

Vallejos, J.A. & McKinnon, S.D., 2013. Logistic regression and neural network classification of seismic records, *Int. J. Rock Mech. Min. Sci.,* **62,** 86–95.

Van Herwijnen, A., Heck, M. & Schweizer, J., 2016. Forecasting snow avalanches using avalanche activity data obtained through seismic monitoring, *Cold Reg. Sci. Technol.,* **132,** 68–80.

Yamada, M., Matsushi, Y., Chigira, M. & Mori, J., 2012. Seismic recordings of the Landslides caused by Typhoon Talas, *Geophys. Res. Lett.,* **39,** L13301, doi:10.1029/2012GL052174, 2012.7.

Yang, H., Zhu, L. & Chu, R., 2009. Fault-plane determination of the 18 April 2008 Mount Carmel, Illinois, earthquake by detecting and relocating aftershocks, *Bull. seism. Soc. Am.,* **99**(6), 3413–3420.

Zhang, Z. & He, S., 2019. Analysis of broadband seismic recordings of landslide using empirical Green's function, *Geophys. Res. Lett.,* **46**(9), 4628–4635.

SUPPORTING INFORMATION

Supplementary data are available at *GJI* online.

Figure S1. The percentages of the maximum frequency (F_m) of all the event types in the training database. See Section 3.3.1 to understand how we separate NRF and MS.

Figure S2. The percentages of the maximum amplitude (A_m) for five event types: (a) percentage of all the events in the database distributed for A_m with a spacing of 1×10^{-5} m s^{-1} and (b) percentage of five event types clustered in spatial A_m ranges of $(-\infty, 1 \times 10^{-4})$, $[1 \times 10^{-4}, 2 \times 10^{-4})$, $[2 \times 10^{-4}, 1 \times 10^{-3})$ and $[1 \times 10^{-3}, +\infty)$.

Figure S3. The distribution of the FFTA ratio (R_{fv}) for all the events in the training database corresponds with the maximum amplitude (A_m); (a) values of R_{fv}, where each event type is represented in a different colour and (b) percentage of R_{fv} for each event type, the results of which are clustered in three ranges: less than 0.5, from 0.5 to 1, and greater than 1.

Figure S4. (a) Linear correlation between E_a and A_m and (b) E_a values of EQ and TR events distributed in three A_m ranges.

Figure S5. (a) Energy variation (R_{ea}) plotted against maximum amplitude (A_m) and (b) the percentages of EQ and RF events with A_m more than 10^{-3} m s^{-1} distributed in the < 0.05 and > 0.05 ranges.

Figure S6. The percentages of five event types distributed according to (a) the maximum frequency ratio (R_f) and (b) maximum amplitude ratio (R_a).

Figure S7. The percentages of EQ and RF events distributed according to the waveform peaks.

Figure S8. The distribution of the event duration from the database; (a) the distribution of all event durations versus A_m and (b) the percentages of EQ, TR and MS events distributed in three different A_m ranges.

Figure S9. The flowchart of classifier C. To_i is the onset time of event i; Te_i is the ending time of event i; e_{i1}, e_{i2}, e_{i3} are the event types classified for the E-W, N-S and Z-Z components, respectively; and E is the event type for one station.

Figure S10. The flowchart of classifier M. E_{12}, E_{12}, E_{13} and E_{14} are the event types classified for seismic stations TOR1, TOR2, TOR3 and TOR4, respectively, and ET is the final event type for the seismic monitoring network.

Figure S11. Frequency spectra of six events and frequency spectrum variation (R_{fv}). The original signals of six events shown in Figs 3(a)–(f) represent EQ, TR, SMS, MS, NRF and ARF events, respectively. The value in each rectangle is the percentage of the energy of that frequency range.

Figure S12. An example of the duration of the N.3 RF event. The time that elapsed between the vertical red and the blue lines is calculated from the first sample triggered by STA = 2 and the last sample triggered by STA = 4.

Figure S13. (a) Original testing signal, (b) detected events in different colours and (c) detection criteria and the onset times automatically detected by DESTRO.

Table S1. The initial and modified weights of five key features for each event type in different feature ranges.

Table S2. The initial weight of each event type calculated for the complementary features.

Table S3. The modified weight of each event type calculated for the complementary features.

Please note: Oxford University Press is not responsible for the content or functionality of any supporting materials supplied by the authors. Any queries (other than missing material) should be directed to the corresponding author for the paper.